

In the format provided by the authors and unedited.

A nanoelectrode array for obtaining intracellular recordings from thousands of connected neurons

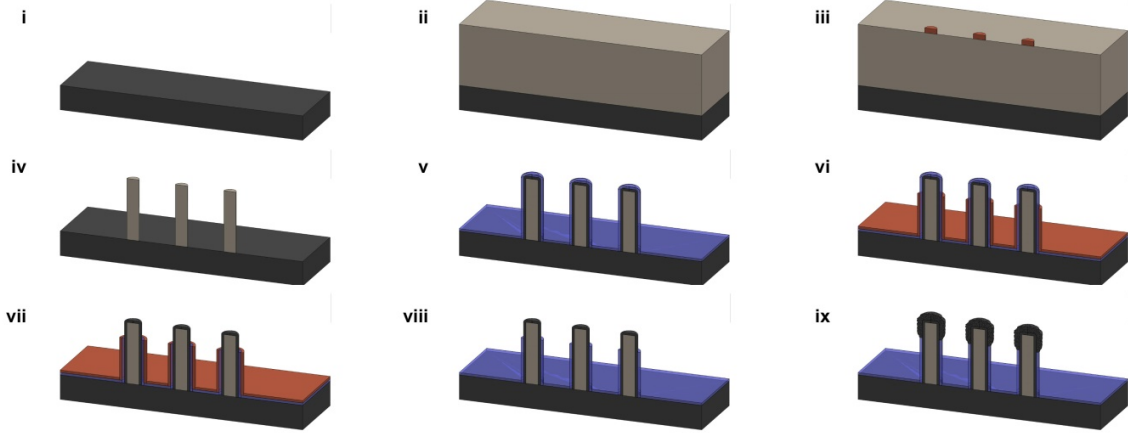
Jeffrey Abbott ^{1,2,3}, Tianyang Ye¹, Keith Krenek¹, Rona S. Gertner², Steven Ban², Youbin Kim³, Ling Qin¹, Wenxuan Wu¹, Hongkun Park ^{2,3*} and Donhee Ham ^{1*}

¹John A. Paulson School of Engineering and Applied Sciences, Harvard University, Cambridge, MA, USA. ²Department of Chemistry and Chemical Biology, Harvard University, Cambridge, MA, USA. ³Department of Physics, Harvard University, Cambridge, MA, USA. *e-mail: Hongkun_Park@harvard.edu; donhee@seas.harvard.edu

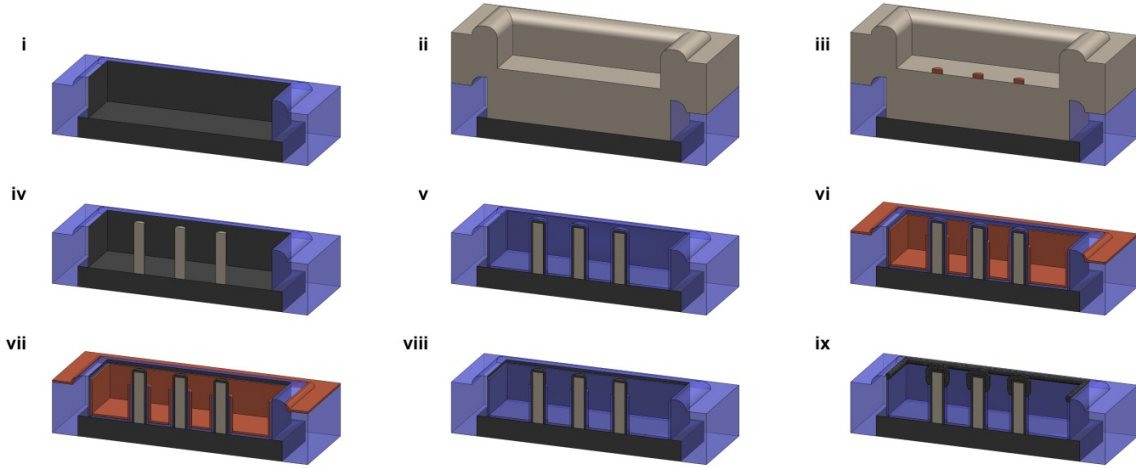
Table of Contents

Supplementary Figure 1 CMOS IC post-fabrication, packaging, and experimental setup.	3
Supplementary Figure 2 Electrodeposition of PtB on the Pt electrodes.	4
Supplementary Figure 3 The CMOS IC and pixel circuit characterization.	6
Supplementary Figure 4 High neuron plating density to form multiple cell layers.	7
Supplementary Figure 5 Threshold I_e magnitude experiments for the pCC configuration.	8
Supplementary Figure 6 Extracellular recording and stimulation of disassociated rat neurons.	9
Supplementary Figure 7 Extracellular amplitudes, IPSPs, and iPSC-derived neuron measurement.	10
Supplementary Figure 8 Additional data analysis of Fig. 2d.	11
Supplementary Figure 9 Simultaneous recording and stimulation in the pCC configuration.	12
Supplementary Figure 10 Typical coupling profiles over time for the pCC configuration.	13
Supplementary Figure 11 Detailed neuron-electrode interface model in the pCC configuration.	14
Supplementary Figure 12 Additional model calculations of the neuron-electrode interface.	15
Supplementary Figure 13 Threshold V_e magnitude experiments for the pVC configuration.	16
Supplementary Figure 14 Intracellular measurements of various signal pathways.	17
Supplementary Figure 15 Intracellular mapping of GDPs due to a drug application.	18
Supplementary Figure 16 Additional synaptic connections.	19
Supplementary Figure 17 Additional examples of spike-triggered-averaged synaptic signals.	20
Supplementary Figure 18 Spike-triggered-averaging and spike cross correlation comparison.	21
Supplementary Table 1. Electrodes fabricated on the CNEI for measuring intracellular signals.	22
Supplementary Discussion 1. Investigating vertical nanoneedle and planar electrode geometries.	23
Supplementary Discussion 2. Intracellular recording and stimulation interface model.	25
Supplementary Discussion 2.1 Experimental Conditions and Circuit Simulation.	26
Supplementary Discussion 2.2 Detailed Circuit Model Derivation.	27
Supplementary Discussion 2.3 Determination of V_{ion}	28
Supplementary Discussion 2.4 Calculation of the Circuit Parameters from Experimental Data.	28
Supplementary References.	30
Supplementary Video Captions.	31
Supplementary Videos 1, 2 Intracellular recordings of neuronal APs across a connected network.	31
Supplementary Video 3 Intracellular stimulation across a neuronal network.	31
Supplementary Video 4 Intracellular mapping of GDPs upon a drug application.	31

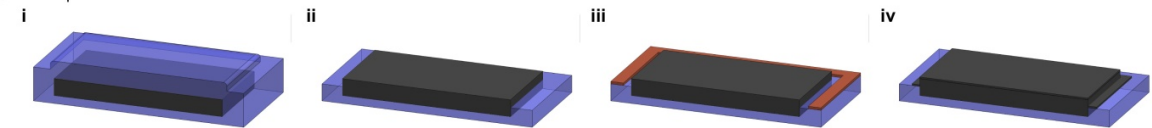
a Vertical nanoneedle electrodes fabrication



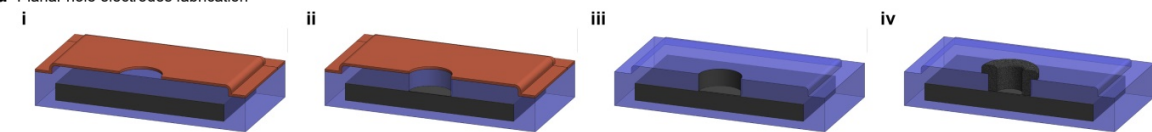
b Vertical nanoneedle with pad edge electrodes fabrication



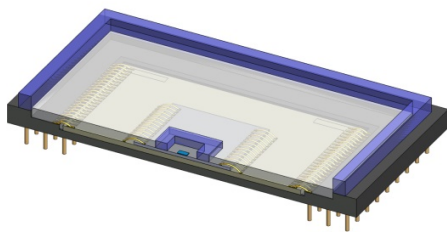
c Planar pad electrodes fabrication



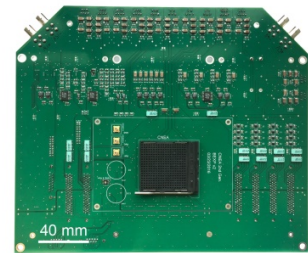
d Planar hole electrodes fabrication



e Device packaging

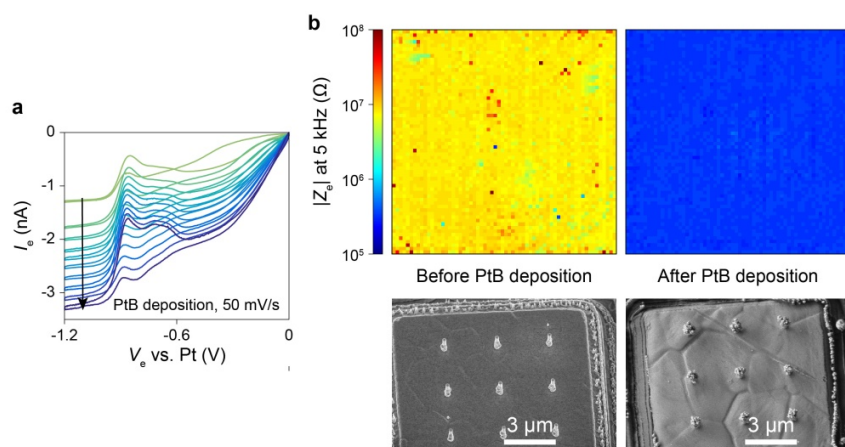


f Experimental setup



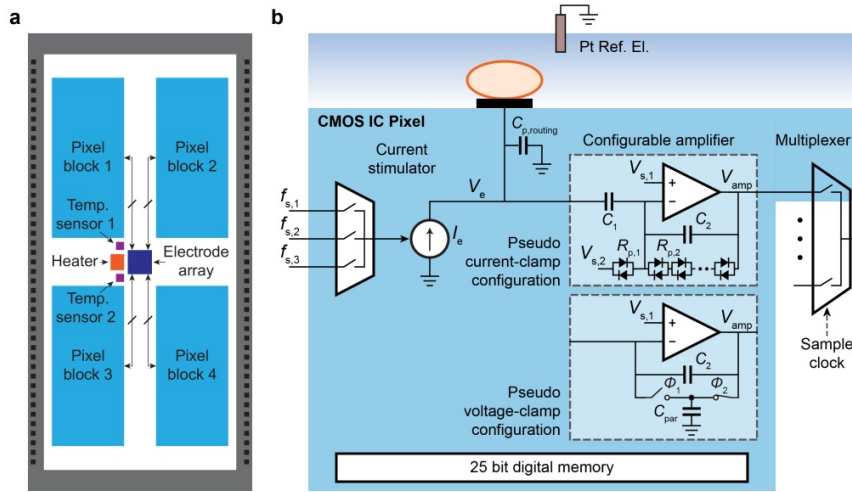
Supplementary Figure 1 | CMOS IC post-fabrication, packaging, and experimental setup.

a, Fabrication steps for vertical nanoelectrodes on aluminum pixel pads of the CMOS IC: (i) Etch foundry passivation and sputter Pt. (ii) Deposit α -Si. (iii) Pattern electron-beam resist etch mask. (iv) Etch α -Si. (v) Conformally deposit Pt and oxide. (vi) Spin-coat etch mask. (vii) Etch oxide to expose Pt. (viii) Prepare device for packaging. (ix) After packaging, see (**e**), electrodeposit PtB. **b**, Fabrication steps for vertical nanoelectrodes with pad edge electrodes are similar to (**a**), except different etch and lift-off masks are used in step (i). **c**, Fabrication steps for planar pad electrodes: (i) Foundry passivation over aluminum pixel pad. (ii) Etch foundry passivation. (iii) Pattern lift-off mask. (iv) Sputter Pt. After packaging, see (**e**), electrodeposit PtB (not shown). **d**, Fabrication steps for planar hole electrodes: (i) Pattern resist etch mask. (ii) Etch foundry passivation. (iii) Sputter Pt. (iv) After packaging see (**e**), electrodeposit PtB. **e**, Packaging is done after post-fabrication of the Pt electrodes but before the PtB electrodeposition. The IC die is epoxied onto an interposer, and the interposer is epoxied onto a ceramic chip carrier. Wirebonds connect the IC to the interposer and the interposer to the ceramic chip carrier. Glass walls (purple) are glued outside of the pixel electrode array onto the IC die and to the outer ridge of the ceramic chip carrier. Polydimethylsiloxane (transparent gray) is poured between glass walls to encapsulate wirebonds. **f**, The device is plugged into a custom designed printed circuit board (PCB) (right) mounted to a microscope stage (left), which interfaces with a data acquisition card and a computer for measurement.

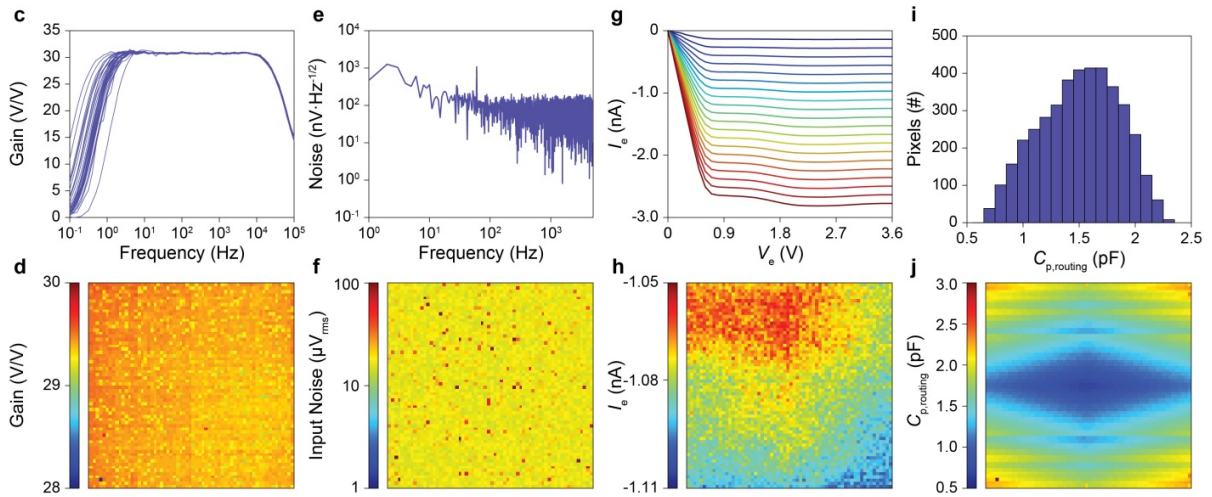


Supplementary Figure 2 | Electrodeposition of PtB on the Pt electrodes.

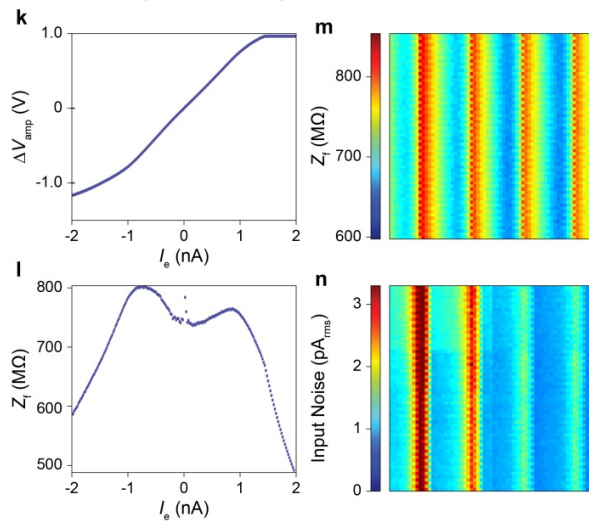
a, A cyclic voltammogram of electrode current, I_e , versus electrode voltage, V_e , during PtB deposition onto a post-fabricated Pt electrode using cyclic electrodeposition with a Pt reference. The impedance of the electrode is reduced with each cycle of deposition, increasing I_e . **b**, (Top) Electrode impedance, Z_e , measurements across the 64×64 array before and after PtB deposition. An impedance reduction of more than 10× is observed. (Bottom) Scanning electron microscopy (SEM) images of vertical nanoneedle with pad edge electrodes before and after PtB deposition. The PtB gives the nanoneedles and the pad edge ridge a nanoscale roughness, which significantly increases the metal-solution surface area, reducing the electrode impedance.



Pseudo current-clamp configuration electrical characterization

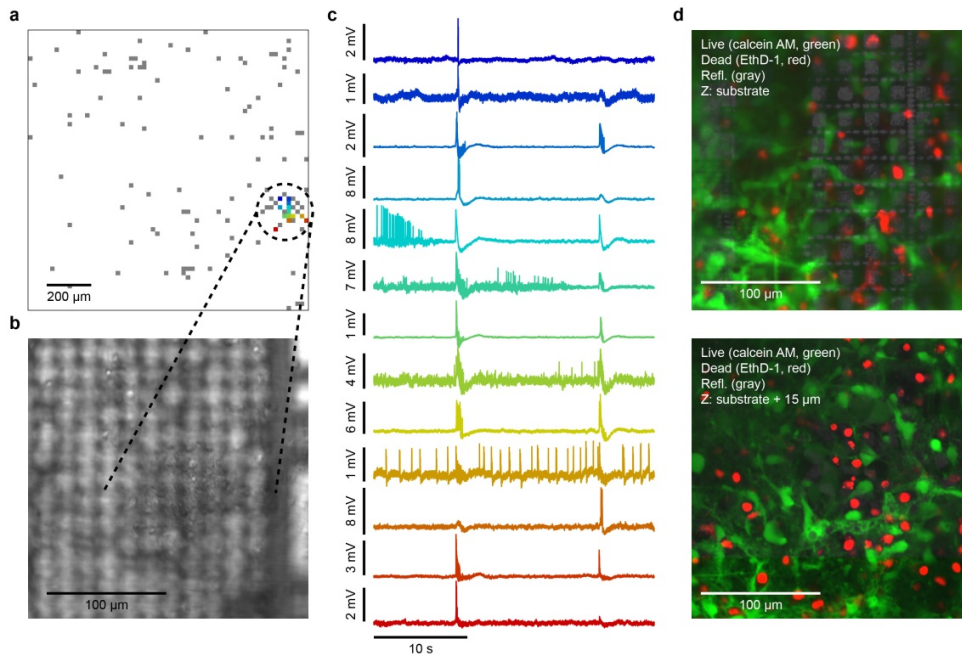


Pseudo voltage-clamp configuration electrical characterization



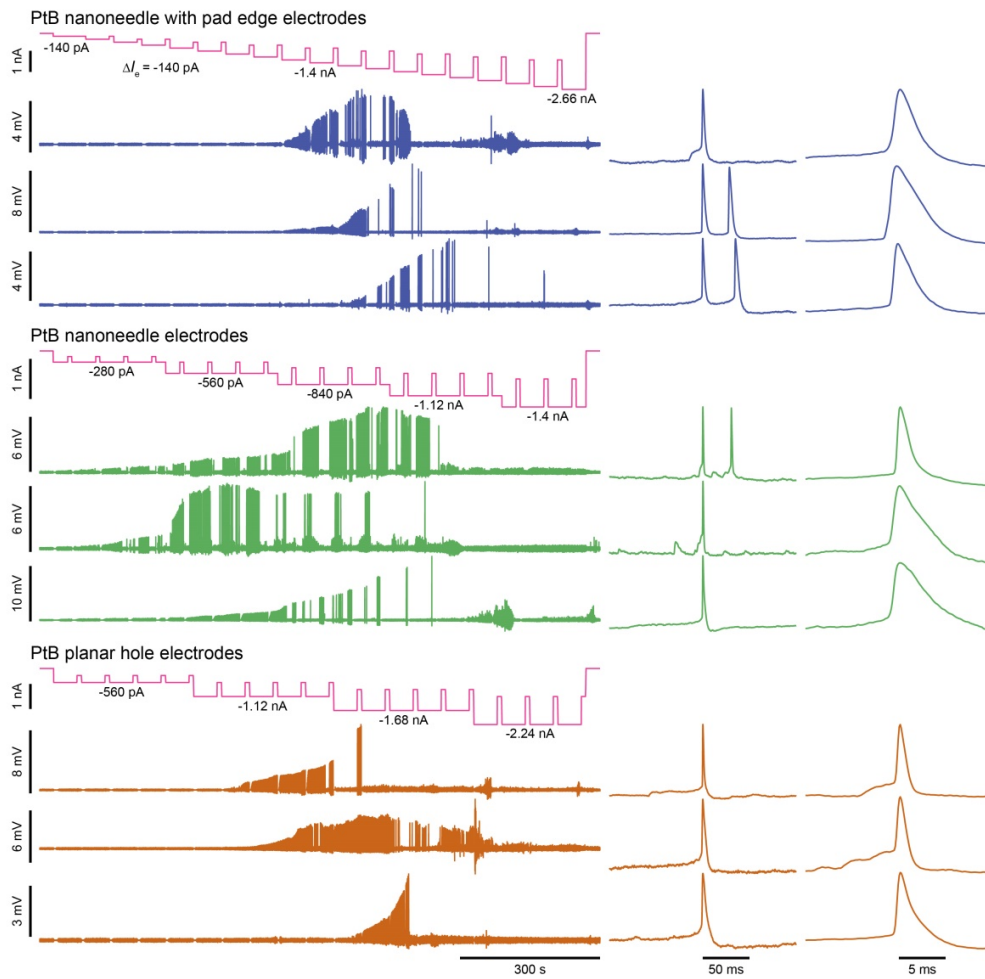
Supplementary Figure 3 | The CMOS IC and pixel circuit characterization.

a, A schematic layout of the CMOS IC. We place the pixel circuits in the four quadrants outside of the pixel pad (electrode) array with routings between pixel pad (electrode) and pixel circuit made in spaces in between. A heater and two temperature sensors are located adjacent to the pad (electrode) array to set the IC's temperature to 34-37°C during experiments. **b**, The pixel circuit contains a switched-capacitor based current stimulator containing a 3:1 input MUX for three different frequency input controls, a configurable single stage amplifier (shown in the two configurations used during intracellular experiments), and a 25-bit digital memory to control the configuration of the stimulator and amplifier. In the pseudo current-clamp (pCC) configuration, the passband gain of the amplifier is set by the ratio of the input capacitance, C_1 , to feedback capacitance, C_2 , where $C_1/C_2 = 3.5 \text{ pF}/110 \text{ fF} \sim 30 \text{ V/V}$. $C_2 \parallel R_{p,2}$ ($R_{p,2}$ is 6 diode pairs in series) sets the low frequency pole below $\sim 1 \text{ Hz}$ whereas $V_{s,1} = 2.2 \text{ V}$, $V_{s,2} = 2.42 \text{ V}$, and $R_{p,1}$ (1 diode pair) are used to adjust the DC value of V_{amp} to maximize dynamic range. In the pseudo voltage-clamp (pVC) configuration, the electrode is directly connected to the negative terminal of the amplifier. The feedback is configured as a switched capacitor, C_{par} , with non-overlapping clock phases φ_1 and φ_2 to generate a impedance, Z_f , of $\sim 750 \text{ M}\Omega$ in parallel with $C_2 = 100 \text{ fF}$, together setting a high-frequency pole of $\sim 2 \text{ kHz}$. **c**, Measured pixel amplifier gain (32 pixels) over frequency for a 1 mV input signal. The pixel sample rate of the 9.4 kHz allows signal measurement up to 4.7 kHz. **d**, Heat map across the 64×64 array of the passband gain at 100 Hz. **e**, Input referred voltage noise of a typical pixel amplifier without solution. **f**, The integrated input referred voltage noise from 1 Hz to 4.7 kHz across the array without solution. **g**, Various magnitudes of the current stimulator's output current, I_e , across its output voltage range, V_e . **h**, Variation of the current stimulator across the array at $I_e = -1.1 \text{ nA}$, typically used during experiments. The array mean $\pm 1 \text{ s.d.}$ is $-1.076 \pm 0.009 \text{ nA}$. **i-j**, Measured parasitic capacitance of the routing between pixel circuit and electrode, $C_{p,\text{routing}}$ in **(b)**, across the array. Each metal trace is designed at a width of 280 nm, a length ranging from $<1 \text{ mm}$ to $\sim 15 \text{ mm}$, and is shielded laterally and vertically by ground to prevent cross-talk between pixels. The attenuation due to this capacitance, $(Z_{p,\text{routing}} \parallel Z_1)/(Z_e + (Z_{p,\text{routing}} \parallel Z_1))$, where $Z_{p,\text{routing}}$ and Z_1 are the impedances of $C_{p,\text{routing}}$ and C_1 , respectively, is small as $|Z_e| \ll |(Z_{p,\text{routing}} \parallel Z_1)|$ due to the PtB deposition. **k**, Transfer function of the amplifier in pVC configuration. **l**, Effective feedback impedance, Z_f , across the tested current range. **m-n**, Feedback impedance **(m)** and the integrated input referred current noise from 1 Hz to 4.7 kHz **(n)** across the array without solution. The vertical stripes are a result of the phase difference between the switched capacitor (switched at 4× the pixel sample rate, 37.6 kHz) and the output multiplexer.



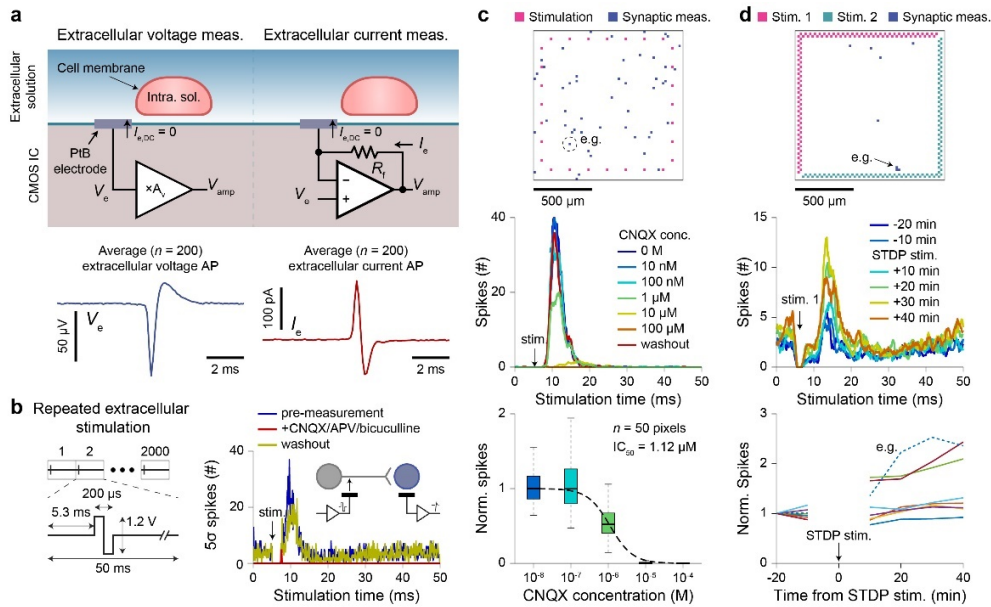
Supplementary Figure 4 | High neuron plating density to form multiple cell layers.

a, A map of the 118 pixels recording intracellular signals (indicated in gray) during an early experiment. An area in the lower right of the array exhibited a high density of intracellularly coupled pixels. **b**, Imaging of this highly coupled area revealed a dense clump of neurons ~6 cell layers high; the remainder of the array had ~1 layer of neurons. After this observation, the plating density was adjusted to form dense 3-6 cell layers of neurons across the whole of the array to couple to most number of neurons. **c**, Example intracellular pseudo current-clamp measurements from this dense region of neurons, color coded by their location in (**a**). Two correlated bursts are observed to propagate across the region. **d**, Live/dead confocal imaging (on the left edge of the array) after intracellular recording from a later experiment was unsuccessful due to these many cell layers preventing the determination of the individual neuron measured from. The substrate is in focus in the top image whereas the top of the cell layers is in focus in the bottom image +15 µm from the substrate.



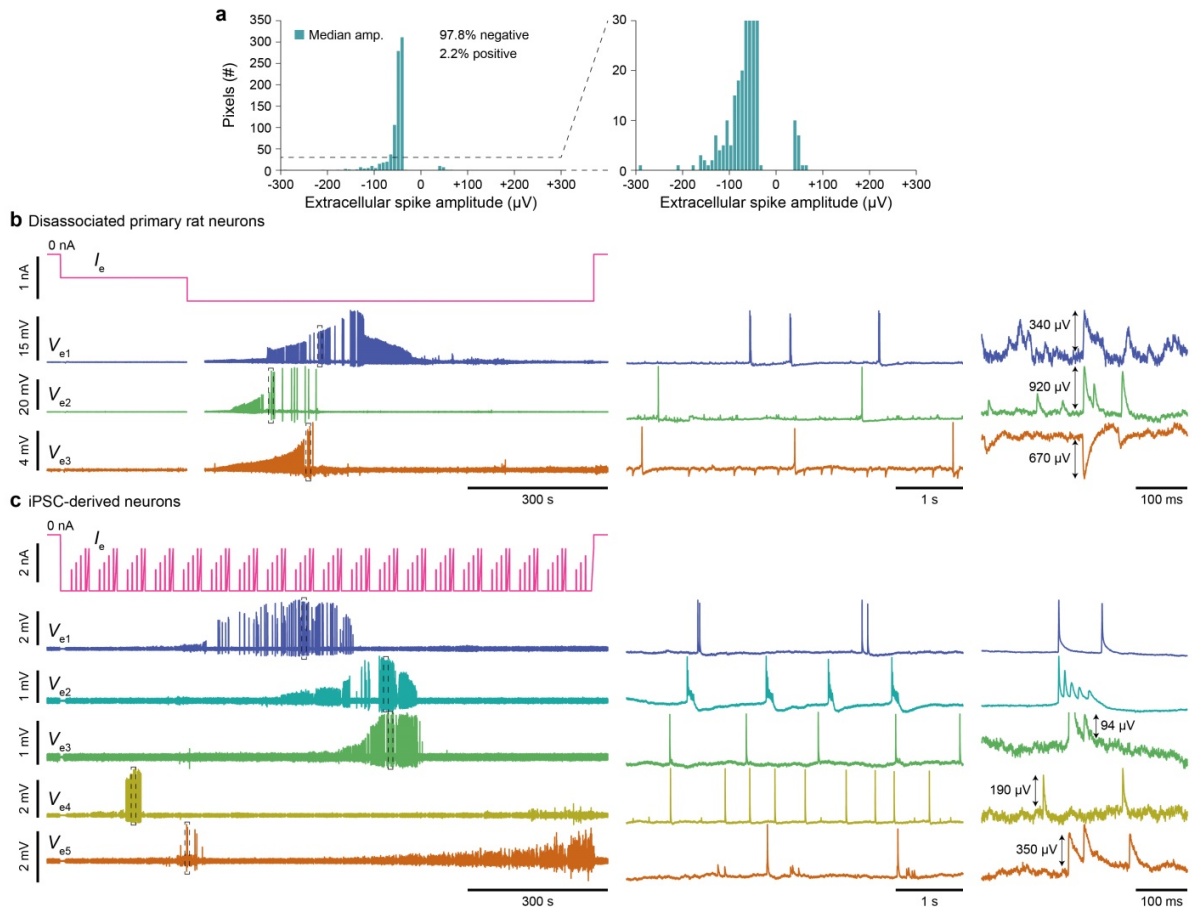
Supplementary Figure 5 | Threshold I_e magnitude experiments for the pCC configuration.

For each electrode type, the magnitude of I_e was gradually increased over a 19 min experiment to determine the threshold I_e needed to attain intracellular access. Further experiments with a single baseline magnitude of I_e were slightly lowered from the threshold value to adjust for any accumulated effects due to the ramped current or were modified to achieve the desired stimulation pattern. Magnified AP waveforms from the peak coupling amplitude of the 19 min trace are shown at the right.



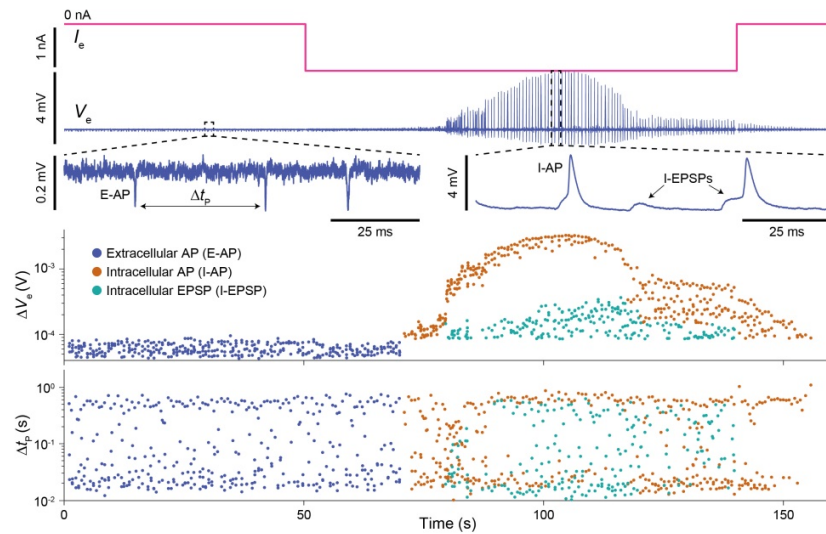
Supplementary Figure 6 | Extracellular recording and stimulation of dissociated rat neurons.

a, Extracellular voltage (left) or current (right) recording can be performed with the configurable pixel circuit with no DC electrode current ($I_{e,DC} = 0$ A). For voltage recordings, the amplifier is configured with a voltage gain, $A_v \sim 300$ V/V; for current recordings, a transimpedance configuration, with a gain $R_f \sim 750$ M Ω , is used. Average ($n = 200$) extracellular action potentials (APs) from the same neuron in both configurations are shown. **b**, Synaptic connections to an extracellularly measured neuron can be stimulated by applying short voltage pulses to other pixels across the array. A peristimulus time histogram (PSTH, histogram bins of 0.1 ms) of the measured neuron's AP spikes (Methods) reveals connections through the jitter associated with network propagation delays and the synaptic integration times (stimulation occurs at 5.3 ms in the PSTH whereas the neuron fires more APs peaking >5 ms after the stimulation). Addition of APV (NMDA antagonist), CNQX (AMPA antagonist), and bicuculline (GABA antagonist) eliminates the stimulated activity. **c**, Extracellular stimulation of selected pixels (top, magenta) excites synapses of measured extracellular neurons (top, blue). Titration of CNQX shows a decrease in the PSTH (middle); changes to the total number of spikes (normalized to 0 M) across 50 pixels measuring a neuron that is synaptically excited (synaptic pixel) reveals the concentration dependence of CNQX (bottom). **d**, Potentiation of synapses is induced through time-delayed stimulation (STDP) protocols. Synaptic pixels (blue, top) are measured using stimulation group 1 (magenta, top) pixels. The PSTH increases (middle) after a STDP protocol of stimulation group 2 being stimulated +10 ms after stimulation group 1 (green, top). The majority of synaptic pixels show an increase in the number of spikes (normalized to -20 min), with three pixels exhibiting >200 % increase in stimulated synaptic activity (bottom).



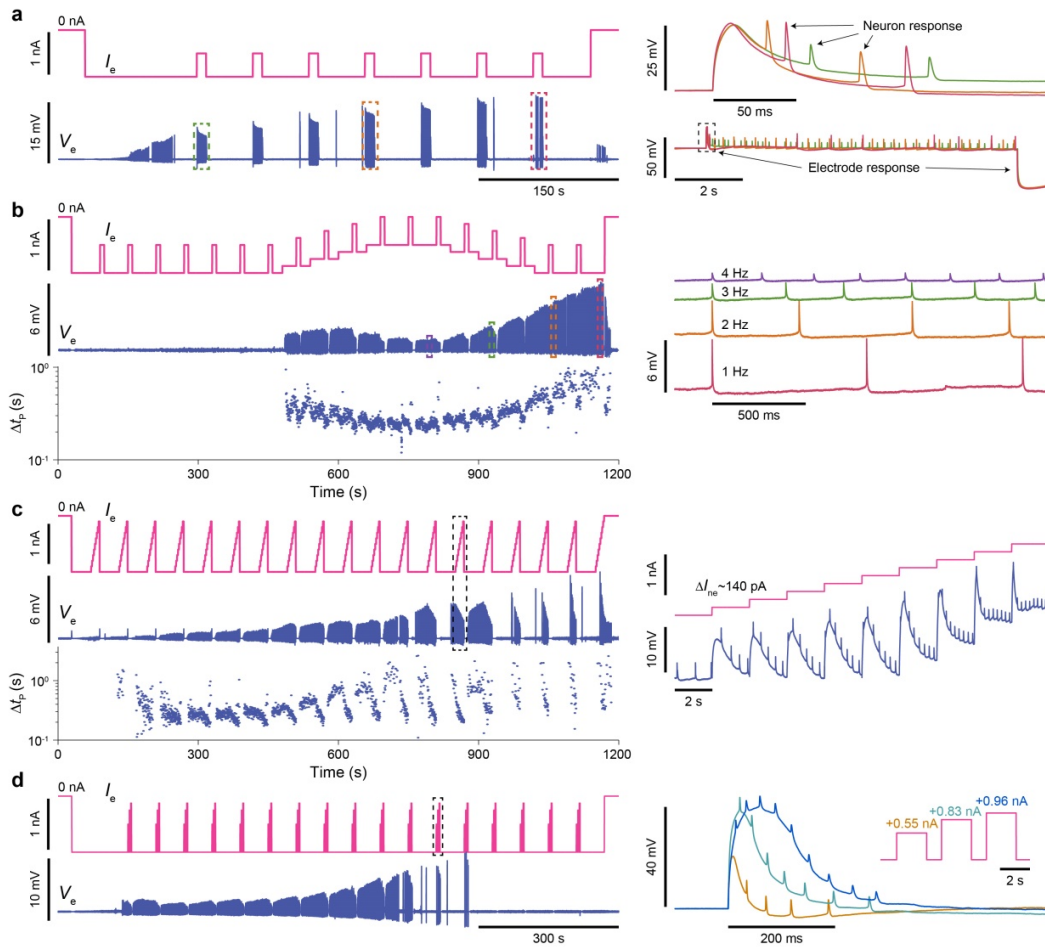
Supplementary Figure 7 | Extracellular amplitudes, IPSPs, and iPSC-derived neuron measurement.

a, Extracellular measurements from an active neuronal culture show that though both positive and negative extracellular spikes are measured with the CNEI, 98% of the measured spikes are negative in polarity. From theoretical simulations of the extracellular potential field around a neuron¹, this suggests that the PtB electrodes interface most strongly with the soma or axon of the neurons as opposed to neurons' dendrites. **b**, Trace V_{e3} shows inhibitory PSPs (IPSPs) measured from disassociated rat neurons using the pseudo current-clamp configuration and $I_e = -1.1$ nA, while traces V_{e1} and V_{e2} show excitatory EPSPs. IPSPs are much less frequent than EPSPs, because young dissociated rat neurons mainly express excitatory synapses. The measured amplitude of the PSPs, as recorded on V_e , are displayed on the right. **c**, Intracellular measurements were achieved using induced pluripotent stem cell (iPSC) derived glutamatergic neurons. Five example traces, V_{e1-5} , from ~ 100 iPSC-derived neurons measured in parallel are plotted using $I_e = -2.9$ nA.



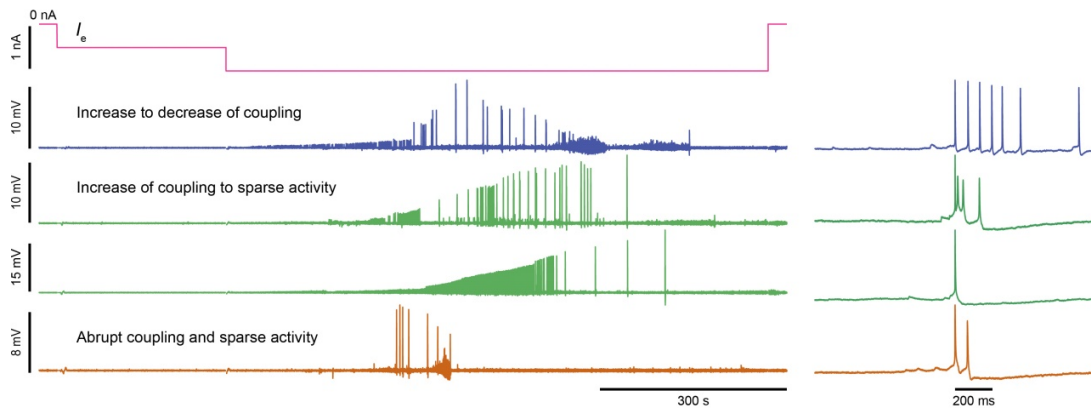
Supplementary Figure 8 | Additional data analysis of Fig. 2d.

Extracellular measurement of a neuron (top) transitions to intracellular measurement by applying $I_e = -1$ nA, resulting in a $\sim 20\times$ improvement in the measured AP amplitude. EPSPs are clearly visible with the increased signal-to-noise. The amplitudes, ΔV_e , of the measured extracellular APs (E-APs), intracellular APs (I-APs), and intracellular EPSPs (I-EPSPs) are plotted in the middle and the times between adjacent APs or AP and EPSP, Δt_p , are plotted on the bottom over the course of the measurement. The burst firing pattern of the neuron, depicted by the two clusters of Δt_p at ~ 500 ms and ~ 20 ms, is maintained before and after the transition of extracellular to intracellular measurement, indicating that the current injection helps to keep the neuron's normal electrophysiological function. At the highest intracellular coupling magnitude, the neuron fires slightly less APs (APs are replaced by EPSPs) possibly due to a hyperpolarization of the resting membrane potential, V_{mp} , whereas during the transition, the AP firing interval decreases for ~ 10 s indicating a possible depolarization with the onset of intracellular access.



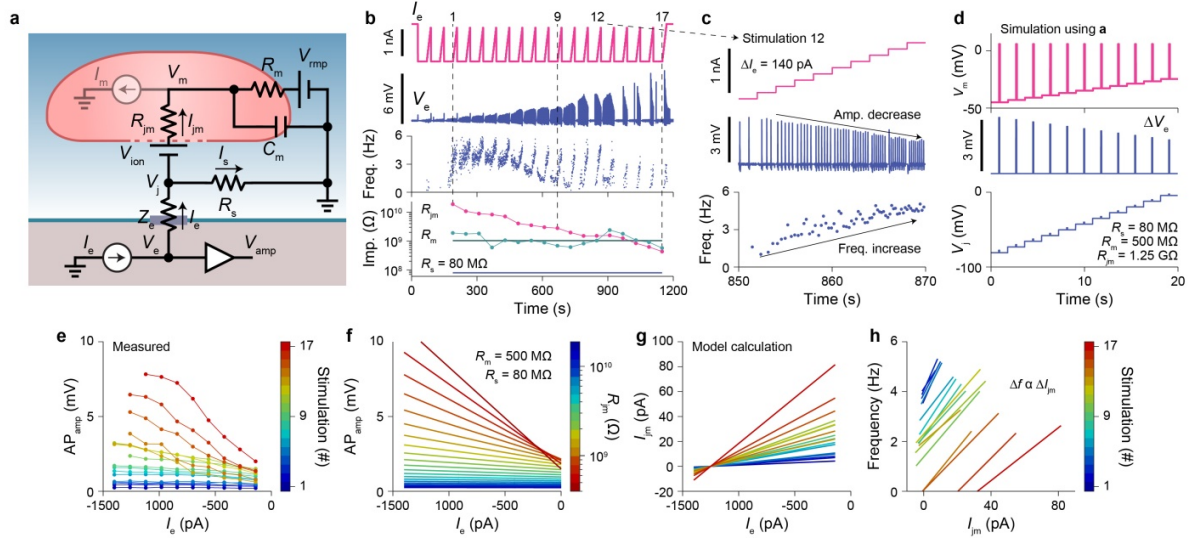
Supplementary Figure 9 | Simultaneous recording and stimulation in the pCC configuration.

a, (supplemental to Fig. 2e) After attaining intracellular access, an effective positive stimulation current can be applied by adjusting I_e to a less negative value: +550 pA injections of 10 s are applied every 60 s over the 600 s recording (top), which excites the neuron to fire APs during the stimulation windows. The electrode also has a voltage response due to the change of I_e but it is much slower than the neuron's and can be removed via a high pass filter (Methods); the electrode's unfiltered voltage response (right, bottom) is clearly distinguishable from the neuron's stimulated APs (expanded view in right, top). **b**, Slow modulation of I_e results in a direct change of firing interval, Δt_p ; example waveforms at various I_e are shown on the right plotted on the same scale. This modulation of Δt_p is most likely due to a modulation of the resting membrane potential, V_{rmp} , at depolarizations above threshold. A relation is also seen for the coupling amplitude and magnitude of I_e , indicating that R_{jm} is lowered by a larger magnitude I_e . Periodic 10 s stimulations of +550 pA every 1 min show a transient decrease in Δt_p . **c**, Faster ramping of I_e results in similar transient modulation of both Δt_p and the coupling amplitude, example waveform shown on right. **d**, Burst firing can be induced when the neuron is normally not firing APs (V_{rmp} hyperpolarized below threshold) by applying pulsed stimulations of increasing magnitudes (I_e shown on right inset). Overlays of pulsed responses show an increasing number of APs with increasing amplitude current stimulations.



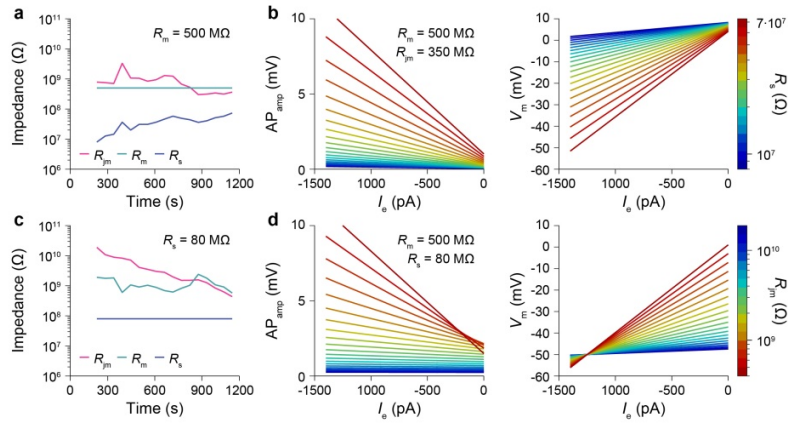
Supplementary Figure 10 | Typical coupling profiles over time for the pCC configuration.

Different types of coupling profiles are typically observed: an increase to decrease in amplitude of coupling (blue), an increase in amplitude of coupling where the neuron activity decreases (green, two examples), and abrupt coupling with sparse activity where there is not a gradual increase in coupling amplitude. Example APs are shown on the right. The green profiles reflect that as the coupling amplitude increases (or R_{jm} decreases), the neuron becomes more hyperpolarized, leading to a decrease in firing activity. The abrupt coupling may indicate that coupling was gained at an already hyperpolarized membrane potential below threshold.



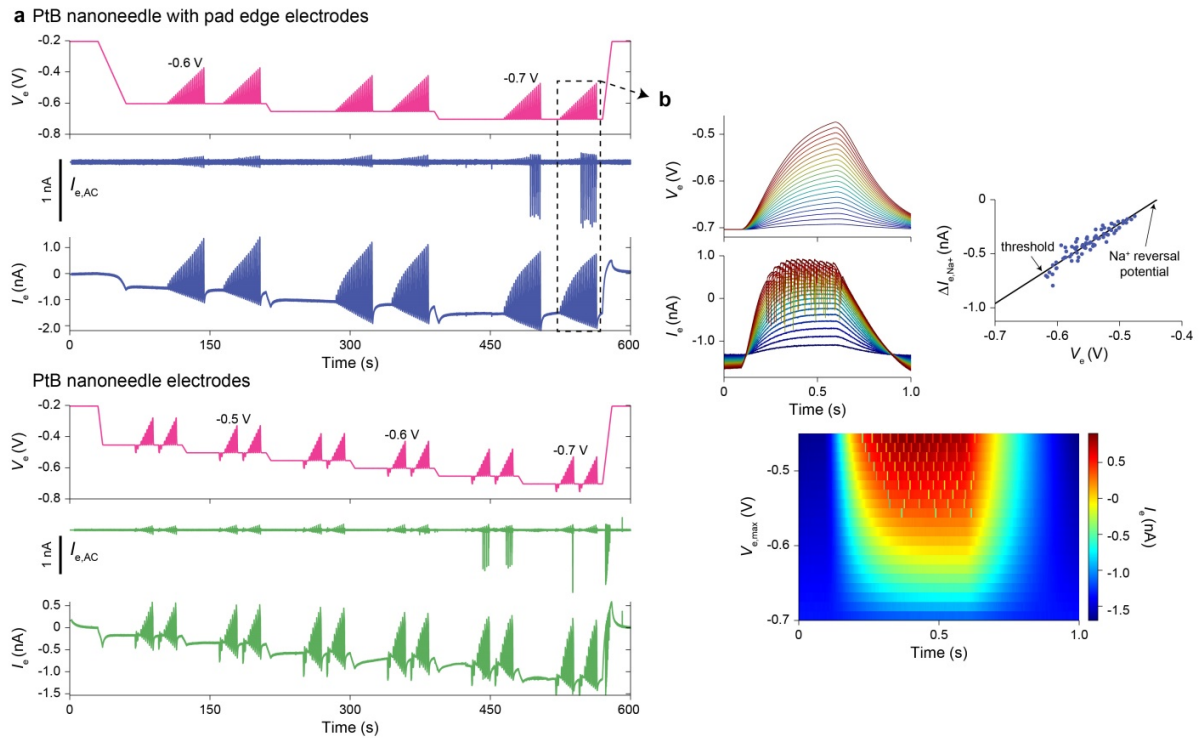
Supplementary Figure 11 | Detailed neuron-electrode interface model in the pCC configuration.

a, A neuron in contact with an electrode is modeled as a junction with a solution potential, V_j . The interfacing membrane is modeled as a junctional membrane resistance, R_{jm} , in series with an ion reversal potential, V_{ion} . The current flowing through the junctional membrane is I_{jm} . The remaining portion of the cell membrane is modeled with a characteristic membrane resistance, R_m , membrane capacitance, C_m , and resting membrane potential, V_{rmp} . The voltage of the intracellular solution of the neuron is the membrane potential, V_m . The electrode, biased in the Faradaic region, is modeled as a nonlinear impedance, Z_e , with a voltage, V_e . The solution gap between the cell membrane and electrode/substrate forms the seal resistance, R_s , with a corresponding seal current, I_s . A high-output impedance current injector with output current, I_e , and a high-input impedance voltage are connected to the electrode to set the electrode current and record its voltage, respectively. V_{amp} is the recorded output voltage after amplification. A membrane current source, I_m , is used for simulation of the neuron as discussed in Supplementary Discussion 2.2. **b**, A series of ramped stimulations are applied every 60 s during a 19 min recording, numbered 1 to 17. The AP firing frequency and a model calculation of R_{jm} and R_m are shown below the recording as discussed in the Supplementary Discussion 2: R_{jm} is calculated to decrease over the course of the experiment enabling the intracellular recording. **c**, During each ramped stimulation, a drop in the measured AP amplitude and an increase in the AP firing frequency are observed. **d**, A model of the neuron firing APs (top) during the ramped stimulation based on the schematic in (a) recapitulates the drop of measured amplitude (middle), V_j is plotted on the bottom trace; model parameters: $V_{AP,max} = +10$ mV, $V_{rmp} = -50$ mV, $V_{ion} = +50$ mV, $R_m = 500$ M Ω , $R_s = 80$ M Ω , $R_{jm} = 1.25$ G Ω . **e**, Over the course of the 17 stimulations, the measured AP amplitude increases and the drop of amplitude during stimulation decreases. **f**, These measured behaviors are reproduced with model calculations assuming a decreasing R_{jm} over the course of the experiment; model parameters: $V_{AP,max} = +10$ mV, $V_{rmp} = -50$ mV, $V_{ion} = +50$ mV, $R_m = 500$ M Ω , $R_s = 80$ M Ω , ~ 20 G $\Omega > R_{jm} > 400$ M Ω . **g**, Calculation of I_{jm} versus I_e during the stimulations shows only a fraction of I_e is injected into the neuron. **h**, Plotting the firing frequency versus the calculated I_{jm} shows an expected direct dependence, further validating the model calculations.



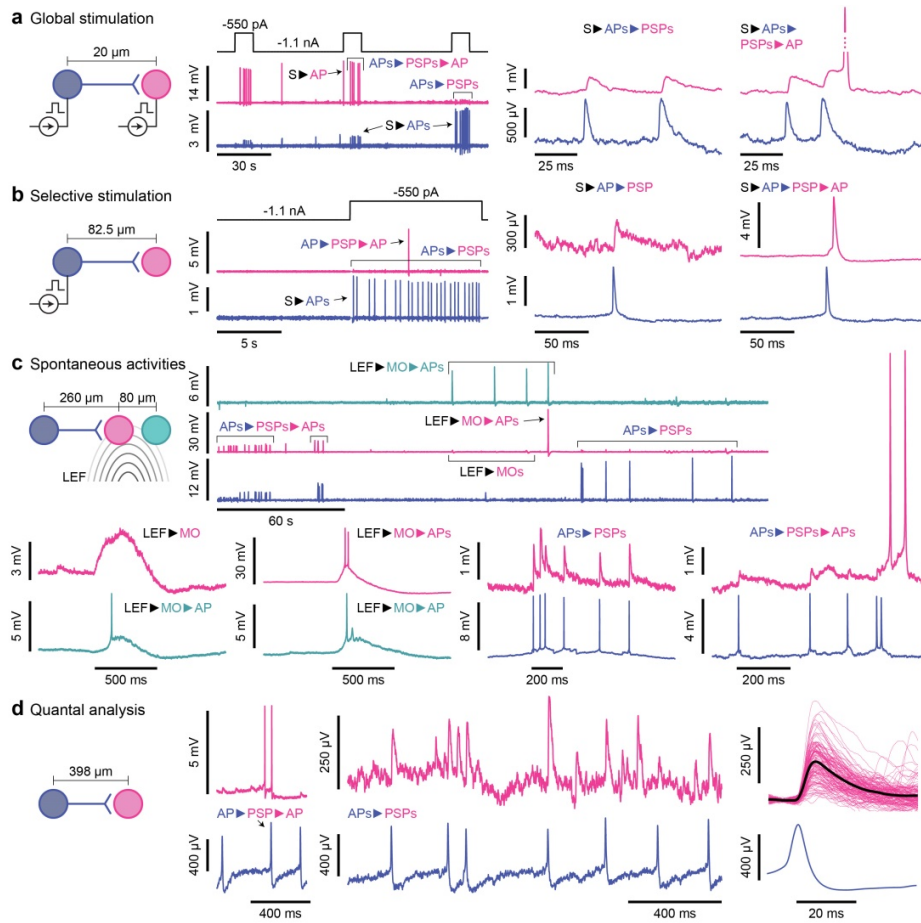
Supplementary Figure 12 | Additional model calculations of the neuron-electrode interface.

a, The calculation of R_{jm} and R_s using Eq. 14 & 15 using [$V_{AP,max} = 10 \text{ mV}$, $V_{rmp} = -50 \text{ mV}$, $V_{ion} = -10 \text{ mV}$, $R_m = 500 \text{ M}\Omega$] and the data from Supplementary Fig. 11e. **b**, Calculations of Eq. 13, left, and Eq. 11, right, using [$V_{AP,max} = 10 \text{ mV}$, $V_{rmp} = -50 \text{ mV}$, $V_{ion} = -10 \text{ mV}$, $R_m = 500 \text{ M}\Omega$, $R_{jm} = 350 \text{ M}\Omega$] and sweeping R_s from $7.98 \text{ M}\Omega$ to $7.35 \text{ M}\Omega$. **c**, The calculation of R_{jm} and R_m using Eq. 14 & 15 using [$V_{AP,max} = 10 \text{ mV}$, $V_{rmp} = -50 \text{ mV}$, $V_{ion} = +50 \text{ mV}$, $R_s = 80 \text{ M}\Omega$] and the data from Supplementary Fig. 11e. **d**, Calculations of Eq. 13, left, and Eq. 11, right, using [$V_{AP,max} = 10 \text{ mV}$, $V_{rmp} = -50 \text{ mV}$, $V_{ion} = +50 \text{ mV}$, $R_m = 500 \text{ M}\Omega$, $R_s = 80 \text{ M}\Omega$] and sweeping R_{jm} from $18.8 \text{ G}\Omega$ to $400 \text{ M}\Omega$.



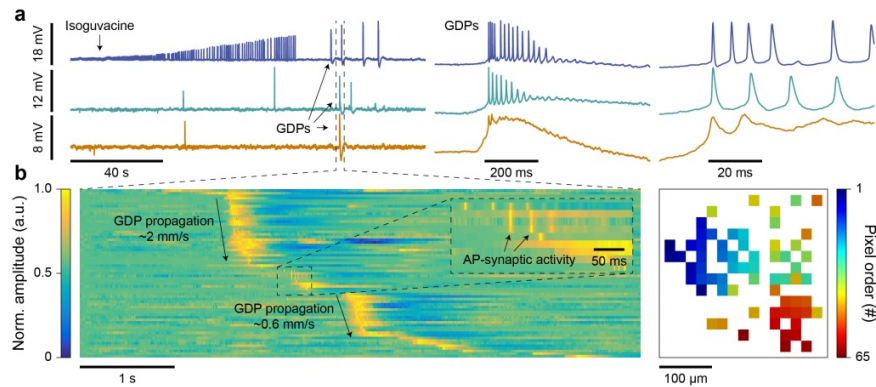
Supplementary Figure 13 | Threshold V_e magnitude experiments for the pVC configuration.

a, For the PtB nanoneedles with pad edge electrodes and PtB nanoneedles electrodes, the magnitude of V_e was gradually increased to determine the threshold V_e needed to attain intracellular access. Activity is only seen during stimulation, clearly distinguished in the high-pass filtered version of the measured electrode current, $I_{e,AC}$. Both electrode types gain intracellular access at an electrode voltage between -0.6 V to -0.7 V at I_e magnitudes corresponding to the measured I_e thresholds, see Supplementary Fig. 5 and Supplementary Table 1. **b**, A direct coupling is observed between V_e and the intracellular potential resulting in a clear stimulation threshold, as visualized in the heatmap plot of I_e (bottom) for different magnitude of V_e stimulations (top, left). The magnitude of the Na^+ spikes is directly proportional to V_e (top, right), indicating a low-impedance resistive interface between the electrode and intracellular solution; an effective threshold voltage and Na^+ reversal potential are identified.



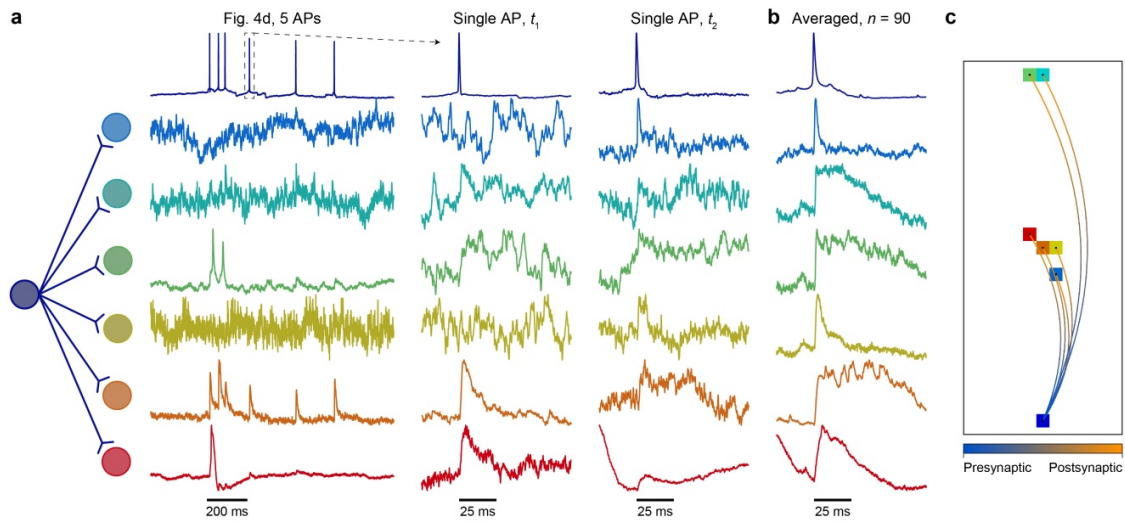
Supplementary Figure 14 | Intracellular measurements of various signal pathways.

a, (supplemental to Fig. 3c) Array-wide stimulation increases the synaptic network activity: stimulated APs of the presynaptic neuron (blue: S▶APs) induce excitatory PSPs in the postsynaptic neuron (magenta, APs▶PSPs). When the PSPs are close enough to summate and exceed threshold, an AP fires (PSPs▶APs). **b**, A synaptic connection can be more specifically excited by stimulating only the presynaptic neuron (blue), which in turn causes excitatory PSPs and an AP on the postsynaptic neuron (magenta). **c**, (supplemental to Fig. 3d) Spontaneous (non-stimulated) membrane potentials of the middle neuron (magenta) can be related to the left neuron via their synaptic connection (blue) and the local electrochemical field (LEF) that also excites the right neuron (green). The LEF induces membrane oscillations (MOs, LEF▶MOs); large MOs cause the neurons (magenta and green) to exceed their thresholds to fire APs (MO▶APs). **d**, (supplemental to Fig. 4a) A mapped connection from the presynaptic neuron (blue) to postsynaptic neuron (magenta) shows varying PSP amplitudes. The summation time (PSP▶AP) is not visible due to the time scaling; ~600 ms is shown for the leftmost data.



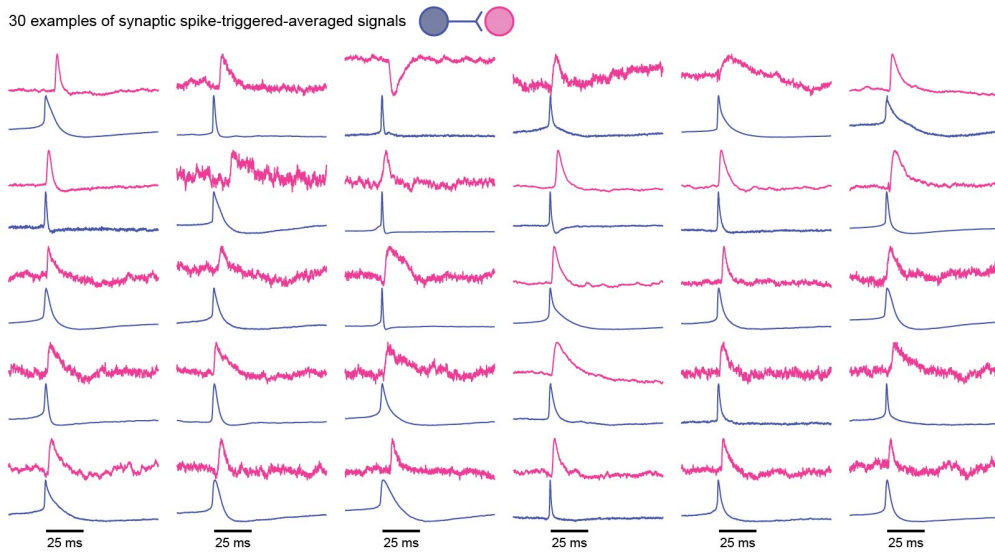
Supplementary Figure 15 | Intracellular mapping of GDPs due to a drug application.

a, The slow nature of the oscillations of Fig. 3d and other recordings (e.g. Supplementary Fig. 4c) closely resemble LEF-induced giant depolarization potentials (GDPs), which can occur in developing neuronal cultures². To confirm this origin, we applied the drug isoguvacine, a GABA synapse agonist, which is known to increase such GDP activity². Indeed, ~1 to 2 min after the drug application, an increase of the frequency of the oscillations was observed accompanied by an increase in magnitude of the depolarizations and burst firing. This experiment confirms that the LEF-induced oscillations are indeed from the same mechanism as LEF-induced GDPs. **b**, A clear spatial propagation of the LEF-induced GDPs is mapped through intracellular measurements from 65 neurons within a $\sim 300 \mu\text{m} \times \sim 300 \mu\text{m}$ area (bottom). Voltage line traces (normalized amplitude) are arranged vertically in the plot (left) and colored in the spatial map (right) based on their first measured electrical activity. Two LEF-induced GDP propagations are observed and indicated with arrows in the voltage trace plot. In comparison to the slow and long LEF-induced GDP propagation of $\sim 1 \text{ mm/s}$, synaptically induced AP activity, shown in the inset, acts on a time scale $\sim 100\times$ faster. Though the presence of these GDPs in young neuronal cultures is well known for creating synaptic connections through “fire together wire together” activity², intracellularly mapping of such propagations with high spatiotemporal resolution has not been possible until now³. See also Supplementary Video 4.



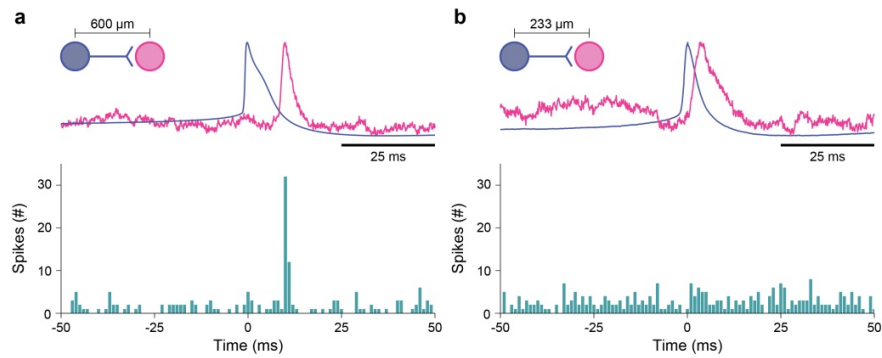
Supplementary Figure 16 | Additional synaptic connections.

a, At least 2 other neurons are also clearly synapsed by the same presynaptic neuron of Fig. 3d with EPSP induced APs observed in the same time window (green and red). A single window around a presynaptic AP is plotted at t_1 to observe subthreshold signals without induced APs. By extending the analysis outside of this time window, a total of 6 postsynaptic neurons are found to have EPSP signals that appear correlated with the presynaptic neuron's APs, visualized in an example 2 min earlier in the data, t_2 . **b**, Performing spike-triggered-averaging (Methods) on the pre-synaptic neuron's APs throughout this 2 min time window ($n = 90$) allows for better resolution of the EPSPs of all six neurons. **c**, These connections are mapped using their pixel locations and an arced line from the presynaptic to postsynaptic neuron's pixel.



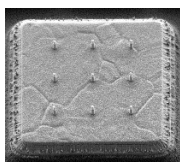
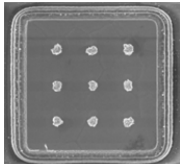
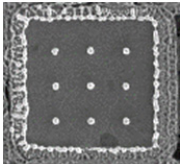
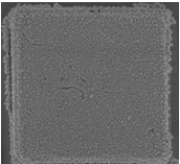
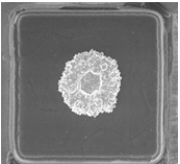
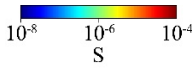
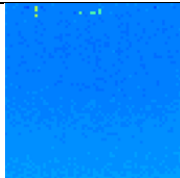
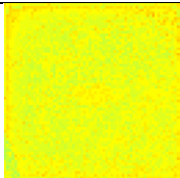
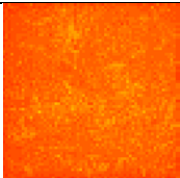
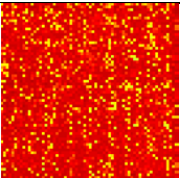
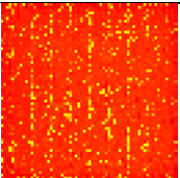
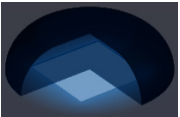
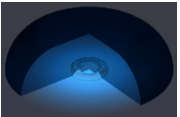
Supplementary Figure 17 | Additional examples of spike-triggered-averaged synaptic signals.

Thirty examples of pre-synaptic and post-synaptic signals from the 304 connections measured in the experiment presented in Fig. 4c-d. (Note: scale bars are omitted due to the variability of the recording attenuation from pixel to pixel and the variation of the coupling amplitude over time; Methods).



Supplementary Figure 18 | Spike-triggered-averaging and spike cross correlation comparison.

a, (Top) Spike-triggered-averaging (Methods) reveals an excitatory connection between a presynaptic (blue) and postsynaptic (magenta); normalized amplitude. (Bottom) The cross-correlogram of the two neurons extracted spike times (Methods) also shows an excitatory connection with a similar propagation delay. **b**, The capability of PSP measurement allows weak synaptic connections to be mapped that are not detected with AP cross-correlation: 304 versus 63 connections are found using spike-triggered-averaging (top) versus spike detection and cross-correlation (bottom).

Electrode geometry	Vertical nanoneedle	PtB vertical nanoneedle	PtB vertical nanoneedle with pad edge	PtB planar pad	PtB planar hole
SEM image of single pixel					
No. of successful pCC intracellular experiments / Total pCC experiments	0 / 5	2 / 2	33 / 34	1 / 1	3 / 4
No. of pixels having measured pCC intracellular signals	0	301	7,800+	2	290
No. of devices	5	2	13	1	4
Typical max pCC intracellular amplitudes (mV)	–	4 – 30	2 – 30	< 0.5	1 – 10
$ I_e $ for intracellular access (nA)	DNE	0.3 – 1.1	1.1 – 2.2	2.2+	0.6 – 1.1
Min $ I_e $ for adverse bubbling with neurons (nA)	0.1 – 0.3	1.1 – 1.4	2.5 – 2.8	> 2.8	1.7 – 2.2
Designed conductance @ 5 kHz $1/ Z_e $ (μ S)	0.03	2	10	40	20
Conductance map across array 					
Thermal kT/C noise (μ V)	67	8.2	3.6	1.8	2.6
Max norm. R_s for single simulated electrode (normalized to the planar electrode)	13	12	< 12	1	3
Three-dimensional R_s simulation with cell interfaced to single electrode 					

Supplementary Table 1. Electrodes fabricated on the CNEI for measuring intracellular signals.

Supplementary Discussion 1. Investigating vertical nanoneedle and planar electrode geometries.

Initial pseudo current-clamp (pCC) experiments with vertical nanoneedle Pt electrodes fabricated on the CNEI showed that passing small Faradaic currents resulted in significant bubbling due to the electrolysis of water at the pixel's electrode with $I_e < 0$. This bubbling was observed to worsen cell health and damage the cell-electrode interface. To reduce this bubbling, we electrodeposited PtB onto the vertical nanoneedle electrodes to increase the metal-solution surface area and reduce the electrode impedance. The voltage required to pass a given current therefore decreases (Supplementary Fig. 2) which also decreases the likelihood of micrometer-scale bubble generation. Beyond preventing bubbles, the reduced impedance also helps to decrease the electrode noise and increase the signal transfer from the solution to electrode, both improving the overall signal-to-noise ratio. Care was taken to produce a high PtB granularity to limit the three-dimensional extent of the vertical nanoneedles so as to preserve the seal resistance benefits of the vertical nanoneedle structure.

After electrodepositing PtB on the vertical nanoneedle electrodes, we were able to successfully record pCC intracellular signals from rat neurons (Supplementary Fig. 5 and Supplementary Table 1); however, we still observed bubbles during current injection at magnitudes that also obtain intracellular access. For example, at $I_e \sim -1.1$ nA, some pixels produced bubbles while other recorded intracellular signals, indicating that the interaction between the neurons and the PtB vertical nanoneedle electrodes is variable and could adversely affect the likelihood of bubbling. To further limit bubble generation, we added an electrode around the pixel pad's outer edge to create the vertical nanoneedle with pad edge electrode geometry. Along with lowering electrode impedance, the PtB pad edge helps shunt a portion of the injection current while the vertical PtB nanoelectrode maintains a high seal resistance for good signal-to-noise ratio recording. After observing the successful recording of intracellular signals with the PtB vertical nanoneedle with pad edge electrode geometry (Supplementary Table 1), we further investigated whether the vertical nanoneedles were required for successful intracellular access by our current injection method. We experimented with PtB planar pad and PtB planar hole electrode geometries whose simpler fabrication processes might prove more attractive to the MEA community. Although the PtB planar pad electrode could record intracellular signals (albeit on two pixels only) with a low likelihood of bubble generation, the signals showed very poor signal-to-noise ratio. The PtB planar hole electrodes, on the other hand, recorded intracellular signals with much better fidelity (Supplementary Fig. 5 and Supplementary Table 1).

Because the PtB vertical nanoneedle with pad edge electrodes consistently measured large intracellular amplitudes with a low risk of bubbling, we performed the vast majority of our experiments with this electrode geometry. Some of these devices could be reused in more than a dozen experiments, accumulating more than 185 non-continuous days *in vitro*. In 33 of our 10-20 minute recordings, the PtB vertical nanoneedle plus pad edge electrodes allowed us to measure intracellular signals from at least one neuron, with an average of ~ 235 intracellular pixels per experiment. We observe that this electrode geometry can measure maximum intracellular amplitudes comparable to those of the PtB vertical nanoneedle electrodes (up to ~ 30 mV amplitudes due to their high seal resistance) and higher than what the PtB planar and PtB planar hole electrodes have recorded.

Beyond a good signal-to-noise ratio, the PtB vertical nanoneedle plus pad edge electrode geometry has the ability to separate the range of injection current magnitudes that achieve intracellular access from those that generate unwanted bubbling. We determined $|I_e|$ for intracellular access in the pCC configuration by gradually increasing its value during an experiment to observe the start and duration of intracellularly-coupled pixels (Supplementary Fig. 5) and for the pseudo voltage-clamp configuration (pVC), we gradually increased the magnitude of the electrode voltage, $|V_e|$ (Supplementary Fig. 13). Similarly, we defined the minimum $|I_e|$ for adverse bubbling by analyzing when pixels start recording characteristic bubbling transients (subsequent experiments showed that this value is influenced by cell density). The inability to define a single $|I_e|$ for these parameters results mostly from the pixel-to-pixel variation of the electrode-cell membrane interactions. We did not thoroughly explore these quantities for the PtB planar electrodes because of their relatively inferior performance.

Electrode conductance is a crucial design parameter that predicts noise contribution and determines the likelihood of bubble generation. Using custom software for cyclic electrodeposition of PtB onto the various electrode geometries, we control the conductance of each pixel and therefore the uniformity across the array (see Methods). The listed conductance values (measured at 5 kHz in phosphate buffered saline $1\times$)

were designed to balance our goal of depositing enough PtB to increase the conductance while limiting the added volume. For example, PtB can be continuously added to an electrode to produce a significantly higher conductance; however, the seal resistance worsens as the PtB grows away from the original electrode surface.

To compare seal resistance across electrode geometries, we simulated a cell interfaced to a single electrode in COMSOL Multiphysics using Electric Currents Physics of the AC/DC Module. In all simulations, a 1 A current was applied through a passivated (with SiO₂) electrode spaced 100 nm from the 50 nm thick cell membrane of a 10 μm diameter cell, and the resulting voltage and equivalent resistance was analyzed. Electrical conductivity and relative permittivity were the same for all simulations, and the results are normalized to the planar electrode seal resistance as it is the smallest. For a more intuitive comparison, we simulated a single contiguous electrode from each geometry for the cell to interact with.

Supplementary Discussion 2. Intracellular recording and stimulation interface model.

We adapt models from previous works⁴⁻⁹ to represent the neuron-electrode interface and to describe intracellular recording and stimulation of neurons using both pseudo current-clamp (pCC) and pseudo voltage-clamp (pVC) electronics, see Supplementary Fig. 11a and Fig. 2a-c with definitions of the circuit components of the model presented in the captions. To gain intracellular access, the impedance of the junctional membrane, modeled as a resistance, R_{jm} , is reduced by applying a negative Faradaic electrode current, I_e , in the range of -0.5 nA to -3.0 nA (determined by Supplementary Fig. 5 for the pCC and Supplementary Fig. 13 for the pVC). The reduction of R_{jm} is attributed to either: 1) hole generation due to electroporation-induced breakdown of the membrane, 2) hole generation due to nanoscale bubbles generated from hydrolysis, or 3) by a gating/opening of the ion-channels in the membrane¹⁰.

In general, a reduced R_{jm} due to I_e enables both recording and stimulation of the neuron's intracellular membrane potential, V_m . For the pCC configuration, with a change of the membrane voltage, ΔV_m , an attenuated version of ΔV_m is generated in the junction solution with a potential V_j ,

$$\frac{\Delta V_j}{\Delta V_m} = \frac{R_s}{R_s + R_{jm}} \quad (1)$$

The electrode potential, V_e , then follows V_j ,

$$\frac{\Delta V_e}{\Delta V_j} = \frac{Z_{p,routing} || Z_1}{(Z_{p,routing} || Z_1) + Z_e} \quad (2)$$

where $Z_{p,routing}$ and Z_1 are the impedances of the parasitic capacitance of V_e , $C_{p,routing}$, and the input capacitance of the amplifier, C_1 , respectively (see Supplementary Fig. 3b), Z_e is the non-linear impedance of the electrode biased in the Faradaic region, and assuming that the output impedance of the current stimulator, $\sim 100 \text{ G}\Omega$, is much larger than the other impedances in the electronics-electrode-neuron interface model. Due to the PtB deposition, $|Z_e| \ll |(Z_{p,routing} || Z_1)|$ resulting in $\Delta V_e = \Delta V_j$, eliminating the attenuation described by Eq. 2. The relationship between V_e and V_m is then simply,

$$\frac{\Delta V_e}{\Delta V_m} = \frac{R_s}{R_s + R_{jm}} \quad (3)$$

For stimulation, a change of the electrode current will generate a change of the membrane potential,

$$\frac{\Delta V_m}{\Delta I_e} = R_s \frac{R_m}{R_{jm} + R_m} \quad (4)$$

assuming that $R_s \ll R_{jm} + R_m$. The benefit of the pCC electronics is the ability to measure ΔV_e and adjust I_e simultaneously, allowing for concurrent recording and stimulation. From Eq. 3 and 4, either a reduction of R_{jm} or an increase in R_s improves both the recording amplitude and the ability to manipulate V_m for stimulation.

For the pVC configuration, a change of the membrane current, ΔI_m , will induce a change of the electrode current,

$$\frac{\Delta I_e}{\Delta I_m} = \frac{R_m R_s}{R_s Z_e + R_{jm}(R_s + Z_e) + R_m(R_s + Z_e)} \quad (5)$$

assuming $|Z_e| \ll R_s, R_{jm}$, and R_m , the transfer function can be simplified,

$$\frac{\Delta I_e}{\Delta I_m} = \frac{R_m}{R_{jm} + R_m} \quad (6)$$

For stimulation, a change of the electrode voltage will induce a change of the membrane potential,

$$\frac{\Delta V_m}{\Delta V_e} = \frac{R_m}{R_{jm} + R_m} \quad (7)$$

assuming $|Z_e| \ll R_s, R_{jm}$, and R_m , and $R_s \ll R_{jm} + R_m$. Similar to the pCC, the pVC electronics enable the ability to measure I_e and adjust V_e simultaneously, allowing for concurrent recording and stimulation. Also similar to the pCC, a reduction of R_{jm} improves both recording and stimulation capabilities. Unlike the pCC, increasing R_s does not improve either the ability to record or stimulate (to a first order

approximation). This is due to the low impedance of Z_e pulling V_j to the pseudo-ground of the amplifier's negative terminal to eliminate shunted current through R_s . It will, however, increase the magnitude of I_e for a given V_e and also decrease recording/stimulation signal transfer if $R_s \sim Z_e$.

To extract the values of R_{jm} and R_s during intracellular access, we performed a set of ramped stimulation experiments in the pCC configuration and simulated the results with the proposed model (see Supplementary Discussion 2.1). The measurements and simulation provide some key insights into the electrode/cell interface and the intracellular coupling mechanism:

1. The trends of the measured data can be best reproduced using the values of $V_{AP,max} = 10$ mV (the AP maximum voltage; see Supplementary Discussion 2.1), $V_{rmp} = -50$ mV, $V_{ion} = +50$ mV, $R_m = 500$ M Ω , $R_s = 80$ M Ω , and 400 M $\Omega < R_{jm} < 18.8$ G Ω .
2. The amount of holding current injected into the neuron, I_{jm} , is only a fraction of applied electrode current, I_e , (e.g. $|I_{jm}| < 100$ pA for $I_e = -1$ nA) and it can be both depolarizing or hyperpolarizing depending upon the values of I_e , R_{jm} , and R_s .
3. With I_e maintained at a constant value, R_{jm} decreases gradually over time to improve the electrode-neuron coupling. The reduced R_{jm} increases the recording amplitude and improves the ability to manipulate V_m for stimulation, as predicted by Eq. 3 & 4.
4. The decreasing R_{jm} causes both the magnitude of I_{jm} to increase and the hyperpolarization of the neuron, which is accompanied by a decrease in AP activity (Supplementary Fig. 11d). This corroborates the most common coupling profile we observed (green traces of Supplementary Fig. 10), where the increase of coupling amplitude is accompanied by a decrease in AP activity.
5. The reduction of R_{jm} is most likely due to the gating/opening of dominantly Na⁺ ion channels: with a negative I_e , the transmembrane potential of the junctional membrane is reduced which causes voltage gated ion channels to open and R_{jm} to decrease.
6. The loss or decrease of coupling, accompanied by a depolarization of the neuron, is most likely due to a decrease in R_s . Due to the slow time scale of the typical loss of coupling being on the order of a minute or longer, we attribute this decrease to a possible clearing of membrane proteins with the current flow through R_s (and the associated electric fields in solution). Sudden decreases of coupling (e.g. V_{e1} in Supplementary Fig. 7b) may be due to a quicker movement of the neuron or membrane.

Supplementary Discussion 2.1 Experimental Conditions and Circuit Simulation.

To investigate the relationships between R_{jm} and R_s during intracellular access, a series of ramped stimulations in the pCC configuration was applied every 60 s during a 19 min recording, numbered 1 to 17 in Supplementary Fig. 11b (also Supplementary Fig. 9c). During each ramped stimulation two trends are observed: a decrease of the measured AP amplitude and an increase of the neuron's AP frequency, Supplementary Fig. 11c. Both effects are attributed to the injected current depolarizing the neuron (V_m becoming more positive) during stimulation (Eq. 4): with V_m rising during the stimulation, and as the action potential maximum voltage is fixed, the intracellular AP amplitude becomes smaller. Therefore, the attenuated recording of ΔV_m using the electrode and current-clamp electronics (Eq. 3), also measures a decreasing amplitude signal (the same trend is also seen in the pVC configuration in Supplementary Fig. 13b). Likewise, it is well known that the AP firing rate of a neuron is roughly proportional to the amount of injected current during stimulation. Therefore, as the amount of injected current increases during the ramped stimulations, the neuron AP firing rate increases proportionally. Beyond a single stimulation, a general trend over the course of all the stimulations shows an increase in the coupling magnitude and larger drops in AP amplitude during stimulation, Supplementary Fig. 11e. These measurements enable us to draw the relationship between circuit parameters and extract their values (Supplementary Discussion 1.2).

A model (e.g. Supplementary Fig. 11d) based on the circuit of Supplementary Fig. 11a and calculated using the data of Supplementary Fig. 11e, shows that all of these observed behaviors can be reproduced with an R_{jm} that slowly decreases over the course of the current injection, Supplementary Fig. 11b bottom. To more clearly elaborate this point, a more simple simulation which sweeps R_{jm} , starting at ~ 20 G Ω and

decreasing to 400 M Ω , and assumes typical values for all the other parameters in the circuit model [$V_{AP,max} = 10$ mV, $V_{rmp} = -50$ mV, $V_{ion} = +50$ mV, $R_m = 500$ M Ω , $R_s = 80$ M Ω] can match the same drop of AP amplitude pattern of the measured data, Supplementary Fig. 11f. Further calculation of I_{jm} , Supplementary Fig. 11g, shows the underlying mechanism: as R_{jm} decreases the amount of injected current increases, which in turn causes larger depolarizations and therefore larger drops in AP amplitude. Plotting the measured firing rate versus this injected current, Supplementary Fig. 11h, shows the direct relationship between the change of the AP firing frequency and the amount of injected current for all stimulations, further verifying the model.

Supplementary Discussion 2.2 Detailed Circuit Model Derivation.

To model the stimulation behavior discussed in Supplementary Discussion 2.1 using the circuit diagram of Supplementary Fig. 11a, a theoretical membrane current source, I_m , is used to depolarize V_m to simulate an AP, where the magnitude of the current is adjusted such that the neuron depolarizes to a maximum value, $V_{AP,max}$. With this model, the effects of I_e on the AP amplitude could then be recapitulated; an example simulation is shown in Supplementary Fig. 11d. Two circuit equations can be expressed for this system:

$$\frac{V_j}{R_s} + \frac{V_j - (V_m - V_{ion})}{R_{jm}} = I_e \quad (8)$$

$$\frac{V_m - V_{rmp}}{R_m} + \frac{V_m - (V_j + V_{ion})}{R_{jm}} = -I_m \quad (9)$$

To solve the needed I_m to drive V_m to $V_{AP,max}$ for an action potential, $I_{m,AP}$, these equations can first be solved for V_m and V_j ,

$$V_j = \frac{R_s[-I_m R_m + I_e(R_{jm} + R_m) - V_{ion} + V_{rmp}]}{R_s + R_{jm} + R_m} \quad (10)$$

$$V_m = \frac{R_m[I_e R_s - I_m(R_{jm} + R_s) + V_{ion}] + (R_{jm} + R_m)V_{rmp}}{R_s + R_{jm} + R_m} \quad (11)$$

$I_{m,AP}$ can then be solved from Eq. 11, where $V_m = V_{AP,max}$,

$$I_{m,AP} = -\frac{R_m(V_{AP,max} - V_{ion}) + (R_{jm} + R_s)(V_{AP,max} - V_{rmp}) - I_e R_s R_m}{R_m(R_{jm} + R_s)} \quad (12)$$

The measured AP amplitude of V_j , or $\Delta V_{j,AP} = \Delta V_{e,AP}$, is then

$$\Delta V_{e,AP} = V_j|_{I_m=I_{m,AP}} - V_j|_{I_m=0} \quad (13)$$

For comparison to the measured data, two expressions can be derived from Eq. 13: the measured amplitude of $\Delta V_{e,AP}$ at $I_e = 0$ and the change of the measured AP amplitude based on the change of I_e ,

$$\Delta V_{e,AP}|_{I_e=0} = \frac{R_s[R_m(V_{AP,max} - V_{ion}) + (R_{jm} + R_s)(V_{AP,max} - V_{rmp})]}{(R_s + R_{jm})(R_s + R_{jm} + R_m)} \quad (14)$$

$$\frac{d}{dI_e} \Delta V_{e,AP} = -\frac{R_m R_s^2}{(R_s + R_{jm})(R_s + R_{jm} + R_m)} \quad (15)$$

These final equations of Eq. 14 & 15 can then be used to compare to the measured data of Supplementary Fig. 11e, where they correspond to the intercept and slope, respectively, of the family curves. By performing linear fits to the data of Supplementary Fig. 11e, two of the six parameters expressed on the right-hand-side of Eq. 14 & 15 can be solved for assuming values for the other four parameters and using the fit parameters to the measured data. In our calculations we assume characteristic values for V_{rmp} and $V_{AP,max}$; in the following section we will explain how we choose V_{ion} and why we choose to fix R_s and solve for R_{jm} and R_m .

Supplementary Discussion 2.3 Determination of V_{ion} .

Any resistance across the membrane, whether ion selective (e.g. K^+ , Na^+ , Cl^- , or Ca^{2+} ion channels) or ion non-selective (e.g. a hole in the membrane), will have an ionic gradient due to the difference in ion concentration between the intracellular and extracellular solutions. To properly model the junctional membrane resistance, the reversal potential of the resistance (modeled as V_{ion} in Supplementary Fig. 11a) needs to be considered which can be solved for using the Goldman-Hodgkin-Katz voltage equation. Two circumstances are considered in relation to our intracellular recording: 1) an ion non-selective hole, representing a hole in the membrane induced either through electroporation or nanoscale bubble generation, and 2) an ion selective hole, representing a gating/opening of the membrane's ion channels. In both cases, standard ion concentrations are considered as shown in the following table.

Ion	Intracellular Concentration (mM)	Extracellular Concentration (mM)
K^+	15	145
Na^+	150	4
Cl^-	10	100
Ca^{2+}	0.0001	1.2

For a passive hole, each ion has an equal permittivity through the membrane. With a gated or opened ion channels such as during an AP, Na^+ has a significantly larger permittivity which causes depolarization. Four calculations of the modified Goldman-Hodgkin-Katz equation¹¹ are shown below relating to a typical resting condition with typical ion permittivity, ion non-selective condition with equal permittivity, ion selective condition with standard AP permittivity, and ion selective condition with just Na^+ permittivity.

Membrane Condition	Relative Permittivity $K^+/Na^+/Cl^-/Ca^{2+}$	Reversal Potential (mV)
Resting	1/0.05/0.45/0.001	-67.3
Ion non-selective	1/1/1/1	-13.1
Ion selective, AP	1/12/0.45/1	+41.1
Ion selective, Na^+	0/1/0/0	+60.6

In solving Eq. 14 & 15 to calculate R_s , R_{jm} , and R_m , we first tried to use $V_{ion} = -10$ mV, to represent ion non-selective openings caused by either electroporation or bubble generated holes in the membrane. Whether we choose to fix R_m or R_s and calculate the remaining two resistances, we inevitably ended up with complex number solutions, meaning that no real values could reproduce the measured data. Adjusting to $V_{ion} = +50$ mV, however, to represent the gating of a majority of Na^+ ion channels, enabled real value solutions. Based on this conclusion, all further calculations therefore used a $V_{ion} = +50$ mV. In terms of the physical processes, the opening of Na^+ channels can be understood in terms of a steady state value of $V_j \sim R_s \times I_e = 80 \text{ M}\Omega \times -1.4 \text{ nA} = -112$ mV, with $V_m - V_j \sim V_{rmp} - V_j \sim +62$ mV. Therefore, the junctional membrane sees a positive transmembrane potential which in turn causes voltage gated ion channels to remain open. From this simple analysis, to achieve intracellular access, $|I_e| \gg |V_{Na} - V_{rmp}|/R_s$ where V_{Na} is the threshold voltage for sodium ion channels; assuming $|V_{Na} - V_{rmp}| \sim 15$ mV and $R_s = 80 \text{ M}\Omega$, $|I_e| \gg 190$ pA for intracellular access. This hypothesis is an extension of a previous study which showed intracellular access to neurons is attainable with an increase of seal resistance possibly latching voltage gated ion channels to stay open¹⁰.

Supplementary Discussion 2.4 Calculation of the Circuit Parameters from Experimental Data.

To calculate R_m , R_{jm} and R_s during an intracellular recording, we use Eq. 14 & 15 and fittings to the measured data of Supplementary Fig. 11e. In the first calculation, we choose to fix R_m and solve for R_{jm} and R_s since R_m , representing the non-junctional membrane, should remain stable during the recording. The result is shown in Supplementary Fig. 12a for $R_m = 500 \text{ M}\Omega$. From the calculation, R_{jm} is relatively stable whereas R_s increases over the course of the recording. Although such an increasing R_s can reproduce the change in AP amplitude, as highlighted in a simplified simulation that fixes $R_m = 500 \text{ M}\Omega$ and $R_{jm} = 350 \text{ M}\Omega$ and sweeps R_s , to produce similar results as the measured data (Supplementary Fig.

12b left), the general trend of V_m , however, shows the neuron would be strongly depolarized during the majority of recording (Supplementary Fig. 12b right), which would prevent normal neuronal function. This data supports that an increase in R_s to reproduce the drop of AP amplitudes during stimulation is unfeasible, as the neuron would be unable to properly function over the course of the whole recording.

To better model the system, Eq. 14 & 15 were instead solved for R_{jm} and R_m with R_s adjusted for values between 1 M Ω to 1 G Ω . The general trend of these calculations was a decreasing R_{jm} and a relatively stable R_m , as shown in Supplementary Fig. 12c for $R_s = 80$ M Ω . A fixed R_s and a decreasing R_{jm} throughout the experiment not only reproduces the measured change of AP amplitude, but it also shows that V_m stays close to V_{rmp} , allowing the neuron to be at a V_m that allows for normal neuronal function. This is shown in Supplementary Fig. 12d where $R_s = 80$ M Ω and $R_m = 500$ M Ω and R_{jm} is swept. In conjunction with a gating/opening of ion channels, the gradual reduction of R_{jm} throughout the recording could relate to a gradual increase in the number of gated/opened ion channels of the junctional membrane or an increase of the portion of the cell membrane becoming gated/opened. Overall, the trends of the measured data could be reproduced using the values of [$V_{AP,max} = 10$ mV, $V_{rmp} = -50$ mV, $V_{ion} = +50$ mV, $R_m = 500$ M Ω , $R_s = 80$ M Ω , 18.8 G $\Omega > R_{jm} > 400$ M Ω]. This model assumes that R_{jm} decreases over the course of the recording due to a gating/opening of a majority of Na⁺ channels as a result of a reduction of the transmembrane potential with a negative I_e . A loss or decrease of coupling is therefore attributed to a decreasing R_s : this would not only lessen the recorded amplitude due to Eq. 3, it would cause a depolarization of the neuron (Supplementary Fig. 12b), and an eventual reduction of R_{jm} as V_j would become more positive and the transmembrane potential would become more negative, closing the Na⁺ ion channels. Due to the slow time scale of the typical loss of coupling being on the order of a minute or longer, we attribute this decrease to a possible clearing of membrane proteins with the current flow through R_s (and the associated electric fields in solution). Sudden decreases of coupling (e.g. V_{e1} in Supplementary Fig. 7b) may be due to a quicker movement of the neuron or membrane.

Supplementary References

1. Obien, M. E. J., Deligkaris, K., Bullmann, T., Bakkum, D. J. & Frey, U. Revealing neuronal function through microelectrode array recordings. *Front. Neurosci.* **9**, 423 (2015).
2. Ben-Ari, Y., Gaiarsa, J., Tyzio, R. & Khazipov, R. GABA: a pioneer transmitter that excites immature neurons and generates primitive oscillations. *Physiol. Rev.* **87**, 1215–84 (2007).
3. Rahmati, V., Kirmse, K., Marković, D., Holthoff, K. & Kiebel, S. J. Inferring Neuronal Dynamics from Calcium Imaging Data Using Biophysical Models and Bayesian Inference. *PLoS Comput. Biol.* **12**, e1004736 (2016).
4. Fromherz, P. Extracellular recording with transistors and the distribution of ionic conductances in a cell membrane. *Eur. Biophys. J.* **28**, 254–258 (1999).
5. Robinson, J. T. *et al.* Vertical nanowire electrode arrays as a scalable platform for intracellular interfacing to neuronal circuits. *Nature Nanotech.* **7**, 180–184 (2012).
6. Spira, M. E. & Hai, A. Multi-electrode array technologies for neuroscience and cardiology. *Nature Nanotech.* **8**, 83–94 (2013).
7. Lin, Z. C., Xie, C., Osakada, Y., Cui, Y. & Cui, B. Iridium oxide nanotube electrodes for sensitive and prolonged intracellular measurement of action potentials. *Nat. Commun.* **5**, 3206 (2014).
8. Abbott, J. *et al.* CMOS nanoelectrode array for all-electrical intracellular electrophysiological imaging. *Nature Nanotech.* **12**, 460–466 (2017).
9. Abbott, J., Ye, T., Ham, D. & Park, H. Optimizing Nanoelectrode Arrays for Scalable Intracellular Electrophysiology. *Acc. Chem. Res.* **51**, 600–608 (2018).
10. Fromherz, P. Self-Gating of Ion Channels in Cell Adhesion. *Phys. Rev. Lett.* **78**, 4131–4134 (1997).
11. Pickard, W. F. Generalizations of the Goldman-Hodgkin-Katz equation. *Math. Biosci.* **30**, 99–111 (1976).

Supplementary Video Captions

Supplementary Videos 1, 2 | Intracellular recordings of neuronal APs across a connected network.

Large network bursts involving 1,837 pixels (Supplementary Video 1) and 1,882 pixels (Supplementary Video 2) are mapped using the spike times and pixel location. The videos are slowed 4× from real time.

Supplementary Video 3 | Intracellular stimulation across a neuronal network.

Network activity is increased across a neuronal network using simultaneous intracellular current stimulations; APs are mapped using the spike times and pixel location. The change of the border color from dark (off) to light (on) indicates the times of the stimulation. The video is slowed 4× from real time.

Supplementary Video 4 | Intracellular mapping of GDPs upon a drug application.

The analog voltages recorded from 65 neurons within a $\sim 300 \mu\text{m} \times \sim 300 \mu\text{m}$ area are visualized ~ 2 min after the application of a gamma-aminobutyric acid synapse agonist to a neuron network. Two giant depolarization potential propagations (GDPs) are observed, with a propagation speed of $\sim 1 \text{ mm/s}$ and a distance of $\sim 200 \mu\text{m}$ (see Supplementary Fig. 15). The video is in real time.